

CENTRAL ASIAN JOURNAL OF THEORETICAL AND APPLIED SCIENCE

https://cajotas.centralasianstudies.org/index.php/CAJOTAS

Volume: 08 Issue: 01 | January 2027 ISSN: 2660-5317

Article

Band-Gap Engineering of $NiCuFe_2O_4$ Spinel via Reed-Derived Activated Carbon: A Sol-Gel Nanocomposite Photocatalyst for Ultrafast Methylene Blue Degradation

Mustafa Q. Jabbar*[1]

1. College of science, University of Tikrit, Tikrit, Iraq
*Correspondence: mustafa.alobaidi@tu.edu.iq

Citation: Jabbar M. Q. Band-Gap Engineering of $NiCuFe_2O_4$ Spinel via Reed-Derived Activated Carbon: A Sol-Gel Nanocomposite Photocatalyst for Ultrafast Methylene Blue Degradation. Central Asian Journal of Theoretical and Applied Science 2027, 8(1), 136-149.

Received: 10th Aug 2026
Revised: 11th Sep 2026
Accepted: 20th Oct 2026
Published: 22th Nov 2026

Copyright: © 2027 by the authors. Submitted for open access publication under the terms and conditions of the Creative Commons Attribution (CC BY) license (https://creativecommons.org/licenses/by/4.0/)

Abstract: In this study, a new and sustainable nanocomposite photocatalyst has been synthesized via the immobilization of $NiCuFe_2O_4$ spinel nanoparticles on reed cellulose activated carbon (RCAC) through a simple sol-gel process. Reed cellulose activated carbon (RCAC) acted not only as a green carbon support but also as a good band-gap modifier for the spinel nanoparticles. Structural, morphological and optical properties of the obtained RCAC/$NiCuFe_2O_4$ nanocomposite have been investigated using UV-Visible diffuse reflection spectroscopy (DRS), X-ray diffraction (XRD), Fourier transform infrared spectroscopy (FTIR), scanning electron microscopy (SEM) and Brunauer-Emmett-Teller (BET) techniques. The efficient loading of RCAC on the spinel structure has led to a significant decrease in the optical band gap of $NiCuFe_2O_4$ from 2.896 eV to 1.566 eV. The optimized RCAC/$NiCuFe_2O_4$ nanocomposite resulted in fast and effective photodegradation of methylene blue (MB), where 97% was attained within 50 minutes at alkaline conditions with pH 10. The degradation kinetics followed a pseudo-first-order rate with a rate constant of 0.0428 min^{-1}. This clearly shows the dual importance of reed-based cellulose activated carbon, as both a green support and a band gap engineer, and proves that RCAC/$NiCuFe_2O_4$ nanocomposites are potential photocatalysts for the removal of organic dye pollutants from wastewater.

Keywords: Photocatalysis; $NiCuFe_2O_4$ spinel; Reed-derived activated carbon; Cellulose; Sol-gel synthesis; Methylene blue degradation.

1. Introduction

Environmental pollution arising from natural and human activities has become a key concern of the twenty-first century, constituting a significant threat to human well-being and marine organisms [1]. Conventionally, chemical contaminants of water have been treated biologically and physically, but these processes are associated with the risk of secondary pollution and are very energy-intensive [2]. Nowadays, photocatalytic degradation technique has become popular among scientists due to the fact that it promises to solve environmental problems thanks to being environmentally friendly, energy-saving, and highly effective [3,4]. Ferrite nanoparticles have recently been considered an important group of materials because of their special properties including high surface area, large surface-to-volume ratio, strong adsorption ability, and easy recovery [5]. Thus, cheap technologies to synthesize and commercialize materials with potential properties obtained from organic solid waste, for example, biomass, are highly

demanded [6]. In reality, organic solid waste including biomass is intrinsically high in carbon, thus these types of waste should be regarded as "resources" [7].

Cellulose is one of the biopolymers that are abundant, renewable, and consist mostly of biomass. Agricultural residues such as corn cobs, banana stems, sugarcane bagasse, and wheat straw serve as sources of cellulose. According to the type of raw material used, lignocellulosic biomass consists of 40-60% w/w cellulose, 15-30% w/w hemicellulose, and 10-25% w/w lignin [8]. Cellulose obtained from biomass is supplied in the form of cellulose fibers. It was reported that the promising composition of agricultural residues, being rich in hemicellulose and poor in lignin compared with the wood, results in more efficient nanofibrillation [9]. Oxide-polymer semiconductor composites can break down organic contaminants to their harmless components under visible-light illumination [10]. Thus, this method is regarded as an effective technique to solve the problem of environmental contamination. Nowadays, due to their biocompatibility, biodegradability, and high photocatalytic activity, composites photocatalysts have gained much popularity [11]. Invention of inexpensive, renewable, and eco-friendly photocatalysts for practical use becomes a global aim towards sustainability [12,13].

MeFe2O4 spinel ferrites (Me=Ni, Co, Cu, Mn, Mg etc.) have such features as stable structure, saturation magnetization, plenty of oxygen vacancies and high density of surface hydroxyl groups [14,15,16]. At the moment, most specialists suggest doping metals by means of using mixed ferrites in order to enhance the catalytic activity of nanoparticles and to increase the interaction between pollutants and nanoparticles [17]. Sharma et al. used La/Cu/Zr trimetallic nanoparticles for the photolysis of AMP and showed that the synthesized nanoparticles had a high photolysis rate of antibiotics [18]. Ibrahim F. et al. [19] and Masoumeh Rahimi et al. [20] used CoMnFe2O4 and ZnCoFe2O4 nanoparticles, respectively, and analyzed their catalytic activity. As in the case with above-mentioned nanoparticles, in the current research, copper-nickel ferrite (CuNiFe2O4) was used as an example of mixed ferrites due to its favorable semiconducting properties and good chemical and thermal stability [17,21]. The combination of NiFe2O4 and CuFe2O4 ferrites in such a nano-sized catalyst allows inducing the transfer of e^- and h^+ [22]. Also, substitution of Cu into $NiFe_2O_4$ can enhance the property of the catalyst like coercivity and saturation magnetization [23]. Catalytic ability of mixed ferrite nanoparticles in aqueous medium is enhanced due to keeping constant the particle size and proper dispersion of the nanoparticles. The carbon material which is obtained from cellulose biomass was used as supporting material having high specific surface area in this study to achieve high loading rate and keep constant the particle size. The carbon material has two major contributions in the enhancement of photovoltaic energy conversion efficiency of photocatalysts; it can decrease the band gap and electron-hole pair recombination rate [24].

2. Experimental

2.1. Materials

Iron(II) nitrate hexahydrate ($Fe(NO_3)_2{\cdot}6H_2O$, 97%), copper(II) nitrate trihydrate ($Cu(NO_3)_2{\cdot}3H_2O$, 99%), nickel(II) nitrate hexahydrate ($Ni(NO_3)_2{\cdot}6H_2O$, 99.99%), ethanol (C_2H_5OH, 99.8%), sodium hydroxide (NaOH, 0.1 M), and sulfuric acid (H_2SO_4, 0.1 M) were purchased from Merck (Germany) and used for the preparation of working solutions and pH adjustment. Cellulose was extracted from common reed (Phragmites australis) plants collected locally. The basic dye methylene blue ($C_{16}H_{18}ClN_3S{\bullet}3H_2O$) was obtained from Merck (Germany). All chemicals used in the present study were analytical grade and were used without any additional purification. Deionized water was used for all experiments.

2.2. Synthesis of $CuNiFe_2O_4$ nanoparticles

$CuNiFe_2O_4$ nanoparticles were synthesized via the sol-gel auto-combustion technique. Briefly, 4 mmol of $Ni(NO_3)_2{\cdot}6H_2O$, 4 mmol of $Cu(NO_3)_2{\cdot}3H_2O$, and 8 mmol of $Fe(NO_3)_3{\cdot}9H_2O$ (Ni:Cu:Fe molar ratio of 1:1:2) were dissolved in 100 mL of deionized

water. This solution was then added dropwise into an aqueous urea solution (16 mmol in 50 mL of deionized water), giving a stoichiometric metal-nitrate-to-urea ratio of 1:2. Subsequently, a 30% ammonia solution was used to adjust the pH to 10. Throughout the procedure, the solution was continuously stirred with a magnetic stirrer at 50 °C and then gradually heated to 90–95 °C under persistent stirring until a viscous green gel was formed. The resulting dried gel was then auto-ignited to yield a loose powder, which was subsequently calcined at 800 °C for 3 h in a furnace and then allowed to cool naturally to room temperature. Finally, the $CuNiFe_2O_4$ nanoparticles were obtained.

2.3. Extraction of cellulose from reed plants and preparation of cellulose-derived carbon

First, the reed plant samples (100 g) were boiled in distilled water (1 L) at 100 °C for 3 h using a reflux system to remove water-soluble impurities. The mixture was then cooled, filtered, and washed with distilled water. Subsequently, The biomass was agitated in a 5% (w/v) NaOH solution at 70 °C for 2 hours. This was followed by filtration and washing with distilled water until neutral pH was obtained. Finally, a bleaching treatment was performed by mixing the sample with a solution consisting of 4% (w/v) NaOH and 7% (v/v) H_2O_2 in a 1:1 volume ratio at 60 °C for 2 h [27]. All treatments were performed in triplicate, and the sample was washed thoroughly with distilled water after each treatment. The resulting ACCell (Activated Carbon derived from Cellulose) was then dried in an oven at 60 °C for 24 h and the dried ACCell was carbonized under a nitrogen atmosphere at 750 °C for 3 h [heating rate in furnace tube (5 °C/min)]. The resulting carbon was ground and sieved through a [0.45 mm] sieve, the activated carbon was stored for further use.

3. Results and Discussions

3.1. Effects of ACCell on bandgap energy of nanocomposites

The bandgap energy of the catalyst is the optical property and the critical element in photocatalytic applications, as it helps in understanding the light absorption property [26]. The DRS spectra of ACCell, $NiCuFe_2O_4$ (NCF) and NCF–ACCell are shown in Fig. 1(a–c). ACCell and NCF–ACCell exhibit intense, broad absorption (≈1.6–1.8 a.u.) from the UV to ~600 nm, followed by a steep absorption edge at ~600–700 nm and a weak tail extending to ~1200 nm. NCF shows markedly lower apparent absorbance (≤0.1 a.u.), a nearly flat visible region, a sharp UV feature near ~220 nm, and a weak band around ~950 nm, which may be associated with d–d transitions of $Fe^{3+}/Cu^{2+}/Ni^{2+}$ in the spinel lattice.

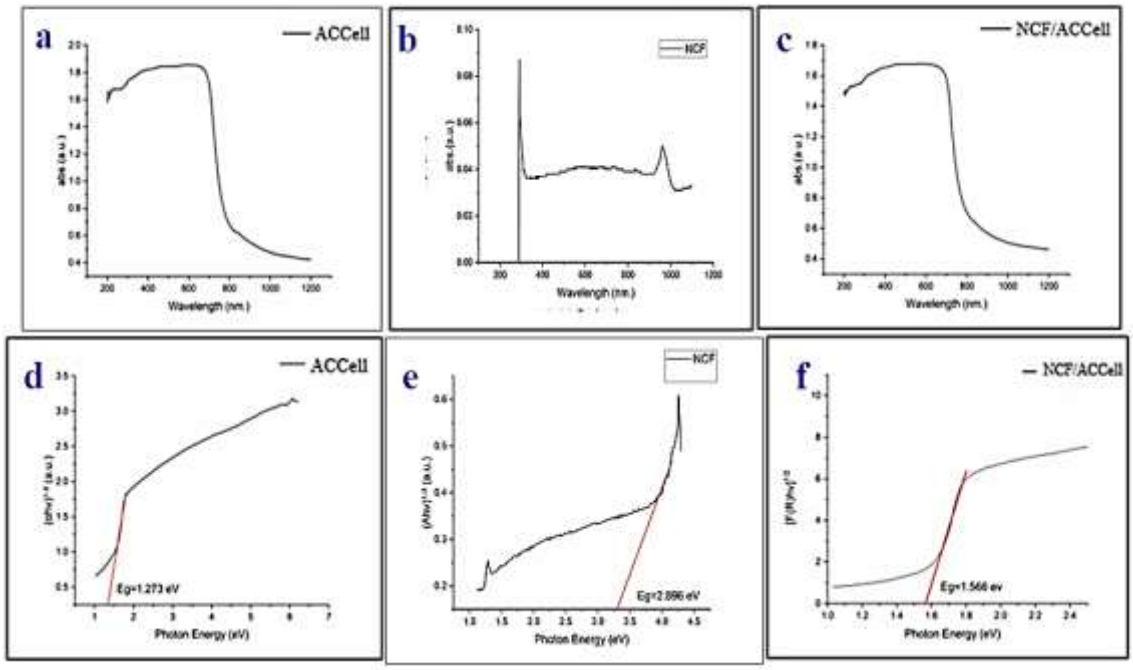


Figure 1. *(a,b,c)* UV–vis DRS spectra & *(d,e,f)* bandgap energy for (ACCell , NCF , NCF/ACCell)

Optical band gaps were estimated from Tauc plots (Fig. 1d–f) using

$(\alpha h\nu)^n \propto (h\nu - Eg)$…….(1)

with n = 1/2 (indirect transition), and F(R) from the Kubelka–Munk function used in place of α for NCF–ACCell, the extrapolated values were 1.273 eV (ACCell), 2.896 eV (NCF) and 1.566 eV (NCF– ACCell). The band gap of the composite lies between those of its components and is ~1.33 eV narrower than that of NCF. Three factors can account for this narrowing. (i) ACCell heat-treated at 750 °C is a disordered, sp^2-rich carbon, whose gap is governed by the size and ordering of $sp^2(\pi)$ clusters rather than by ACCell itself [27]. Its π/π^* states are positioned halfway through the ferrite gap; therefore, it acts like a narrow bandgap material. (ii) Interaction at the interface between the carbon surface (functionalized oxygen) and Fe/Ni/Cu ions may generate Fe–O–C bond structures, resulting in the formation of interface and defects states that manifest themselves as sub-bandgap absorption, causing a reduction in Eg [30]. (iii) Carbon matrix prevents agglomeration of the ferrite, thus increasing its dispersion and light access [31]. Similar narrowing has been reported for ferrite/carbon systems such as $NiFe_2O_4$/MWCNTs [32] and $NiFe_2O_4$/g-C_3N_4 [34]. The narrower gap extends visible-light harvesting, and the conductive carbon can also act as an electron acceptor that suppresses e^-/h^+ recombination, which is favorable for photocatalysis.

3.2. XRD and FT-IR analysis

The XRD pattern of ACCell(Fig. 2a) exhibits two broad humps centered at $2\theta \approx 22°$ and ≈ 43°, which are assigned to the (002) and (100/101) reflections of turbostratic, poorly graphitized carbon [1]. The characteristic crystalline ACCell reflections at ~15°, ~16.5°, and ~22.6° are absent, indicating a complete loss of the native ACCell crystal lattice after thermal treatment. The (002) maximum corresponds to an interlayer spacing of ≈ 0.40 nm (Bragg's law, Cu Kα), which is larger than that of ideal graphite (0.335 nm) and reflects a disordered arrangement of small aromatic layers.

NCF (Fig. 2b) exhibits sharp reflections at $2\theta \approx 30.2°$, 35.6°, 43.2°, 53.5°, 57.2°, and 62.8°, which are indexed to the (220), (311), (400), (422), (511), and (440) planes of a cubic spinel structure (Fd-3m), in agreement with $NiFe_2O_4$ (JCPDS 10-0325). The sharp (311) peak indicates good crystallinity, while a broad hump in the range of 20–30° may indicate a small contribution from the amorphous phase. Crystallite size can be calculated by the

Scherrer equation, $D = 0.9\lambda/(\beta \cos\theta)$ [4], taking into account the (311) reflection in instrumentally corrected data.

In the NCF/ACCell composite (Fig. 2c), all spinel peaks remain in their initial positions; moreover, a small broad hump is observed at ~24°. This means that ferrite phase remained unchanged, no new crystalline phase was formed, and cellulose-based carbon remains amorphous in the composite. Reduced intensity of this carbon hump compared to the ACCell case is probably due to the fact that the highly crystalline ferrite phase diluted carbon content. Thus, the idea that NCF and carbon were linked via interface is more reasonable.

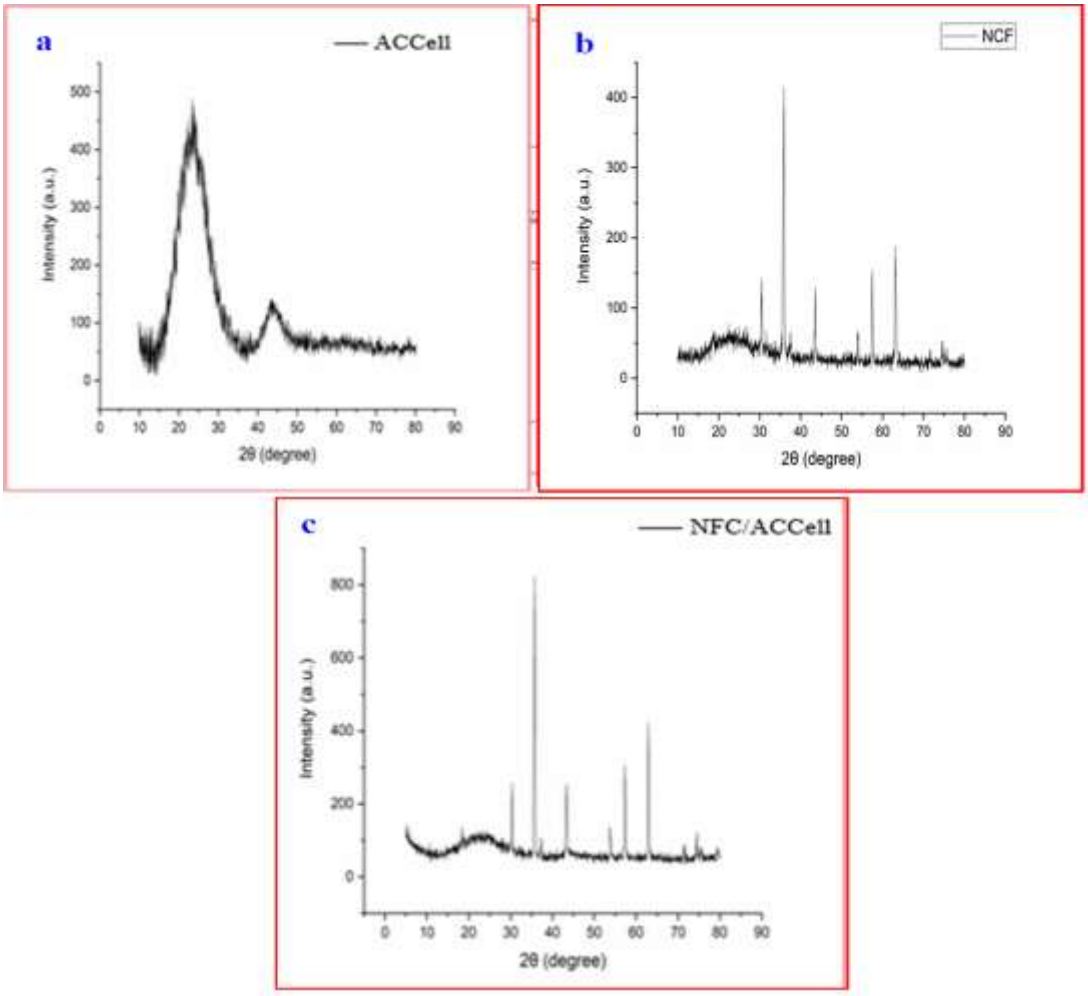


Figure 2. XRD patterns of a) ACCell, b) nano NCF c) NFC/ACCell nanocomposite

In the FT-IR spectrum of NCF, the strong band at 590 cm^{-1} is attributed to the intrinsic stretching vibration of metal–oxygen bonds at tetrahedral sites (ν_1), while a second band below ~450 cm^{-1} corresponds to octahedral-site M–O vibrations (ν_2). These two bands are characteristic of the spinel structure. The bands at 3437 and ~1624 cm^{-1} arise from O–H stretching and H–O–H bending of adsorbed water, respectively. Weak bands at 2916 and 1722 cm^{-1} are assigned to C–H and C=O vibrations of residual organic species from the synthesis. The IR spectrum of ACCell shows a broad O–H stretching region (3300–3450 cm^{-1}), aliphatic C–H stretching at 2920 and 2847 cm^{-1}, a band at 1628 cm^{-1} (aromatic C=C and/or adsorbed water), a band at 1408 cm^{-1}, and C–O/C–O–C stretching bands at 1109, 1092, and 1055 cm^{-1}. The retention of oxygenated groups on a carbon framework whose XRD pattern shows no ACCell lattice indicates an oxygen-functionalized, partially carbonized surface. Such groups are potential anchoring sites for metal cations.

The NCF/ACCell spectrum (Fig. 3) combines features of both components: the tetrahedral M–O band at 592 cm^{-1} and the octahedral band at 465 cm^{-1} of the spinel,

together with O–H (3439 cm^{-1}), C–H (2924 cm^{-1}), C=O (1722 cm^{-1}), C=C/COO^- (1576 cm^{-1}), CH_2/COO^- (1456 and 1383 cm^{-1}), and C–O (1105 cm^{-1}) bands of the carbon matrix. The coexistence of both sets of bands confirms the formation of a composite. The 2 cm^{-1} shift of the M–O band relative to NCF (590 → 592 cm^{-1}) lies within the instrumental resolution and is therefore not interpreted as evidence of interfacial bonding.

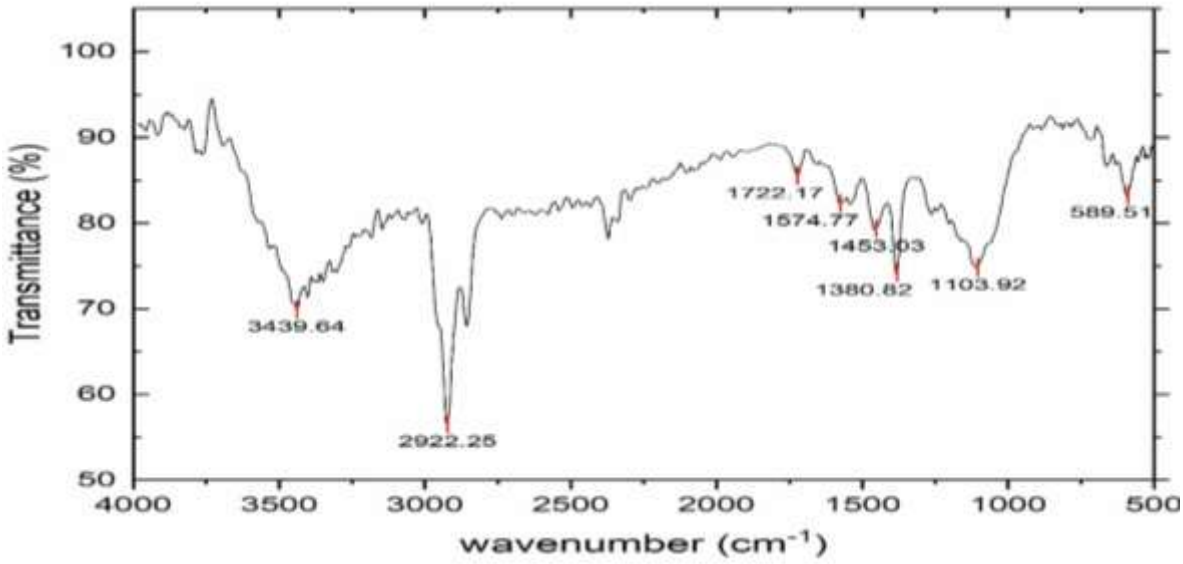


Figure 3. FTIR spectra of NCF/ACCell nanocomposite.

3.3. Morphology and elemental composition

The surface morphology and elemental composition of pristine ACCell, $NiCuFe_2O_4$, and the $NiCuFe_2O_4$/ACCell nanocomposite were probed using field-emission scanning electron microscopy (FE-SEM) coupled with energy-dispersive X-ray spectroscopy (EDS) and elemental mapping (Figs. 4 and 5). Pristine ACCell consisted of elongated, parallel fibrous bundles accompanied by fragmented fibers and irregular debris, some of which showed regularly arranged micro-perforations characteristic of plant cell-wall pits (Fig. 4b). This observation was supported by the EDS analysis, which revealed only C (96.39 wt%) and O (3.21 wt%), together with a trace of Cl (0.40 wt%) attributed to residues from the extraction or bleaching steps. C and O mapping followed the shape of the fibers, while Cl mapping showed a random distribution not following the shape of the fibers (Fig. 5a).

There were no Fe, Ni, and Cu signals observed, proving the suitability of the ACCell material as a blank for the composite material. On the other hand, $NiCuFe_2O_4$ nanoparticles possessed the quasi-spherical structure with agglomerated grains. The measured particle diameters were 26.19, 37.04, and 42.75 nm (average ≈ 35 nm), confirming their nanoscale dimensions. The agglomeration is attributed to the high surface energy and magnetic dipole–dipole interactions among the ferrite particles, while the voids between the grains are likely due to the release of gases during synthesis.

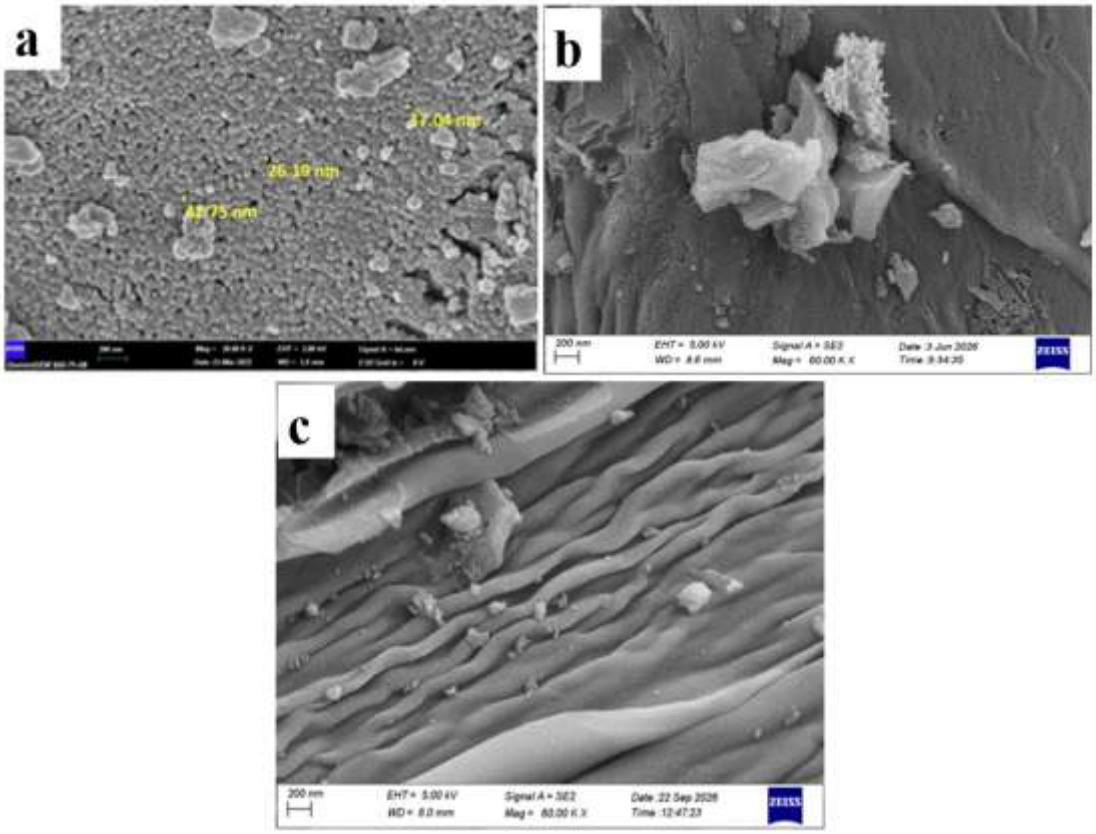


Figure 4. FE-SEM micrographs along with their respective magnifications showing (a) NCF nanoparticle, (b) ACCell, and (c) NCF/ACCell nanocomposite.

The EDS spectrum of $NiCuFe_2O_4$ showed the characteristic Fe, Ni, and Cu peaks (Fe Kα ≈ 6.4 keV, Ni Kα ≈ 7.47 keV, and Cu Kα ≈ 8.04 keV) together with a strong O peak, confirming the formation of the mixed Ni–Cu–Fe oxide (Fig. 5). The elemental maps (200 μm scale bar) showed a dense and continuous distribution of the detected elements, with no segregated phases, indicating a homogeneous composition at the micro-scale. The ACCell/$NiCuFe_2O_4$ nanocomposite retained the fibrous architecture of ACCell but had a markedly rougher and uneven surface, with undulations, longitudinal fissures, and particulate deposits adhering to the fibers. At higher magnification, the fiber surface was uniformly covered by a nano-textured layer of $NiCuFe_2O_4$ particles with sizes ranging from 15.28 to 96.49 nm (average of the fine features ≈ 46 nm), together with a few larger aggregates of about 264 and 324 nm.

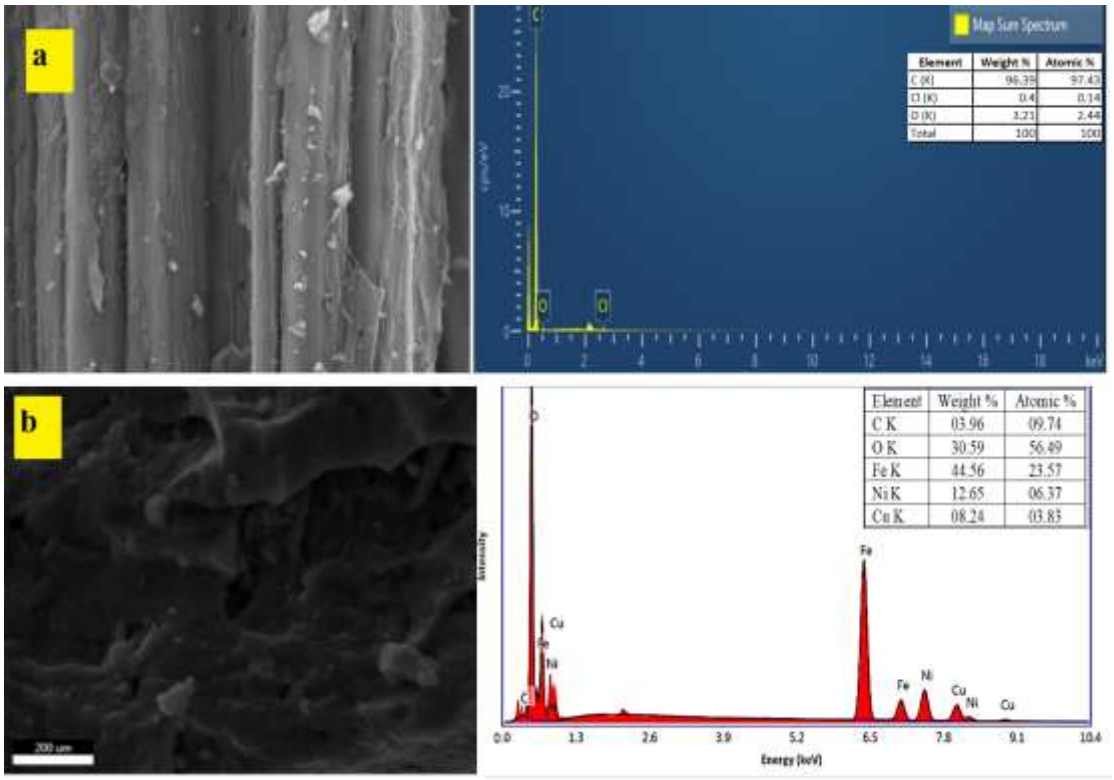


Figure 5. EDX spectrum and selective area mapping micrographs for elemental distribution of (a) ACCell; (b) NCF/ACCell

The smaller size of most particles on the ACCell compared with free $NiCuFe_2O_4$ suggests that the hydroxyl-rich ACCell network acted as a template that limited particle growth and agglomeration through hydrogen bonding and electrostatic interaction with the metal cations (Ni^{2+}, Cu^{2+}, and Fe^{3+}).

The EDS analysis supported this, as the composite showed Fe (0.81 wt%) and Cu (0.37 wt%) in addition to C (93.12 wt%) and O (5.37 wt%), with trace Cl (0.22 wt%) and Si (0.11 wt%) attributed to precursor or handling impurities (Fig. 7). The increase in the O content relative to pristine ACCell (from 3.21 to 5.37 wt%) is consistent with the contribution of the metal–oxygen lattice. The maps showed that C and O defined the fibrous bundle, Cu was dispersed finely and uniformly over the fiber, and Fe was scattered over the fiber with a few localized clusters of a few micrometers. These clusters are consistent with the larger aggregates observed by SEM. The layered EDS image confirmed that the metal signals were spatially associated with the ACCell fibers, which supports anchoring of the ferrite on the ACCell surface rather than a physical mixture. The Fe:Cu atomic ratio was about 2.6:1, close to the nominal ratio of the ferrite, and the low overall loading (Fe + Cu ≈ 1.2 wt%) is expected for a thin ferrite coating on a bulk organic support. However, Ni was not detected in the acquired EDX spectrum. This may be associated with its low local concentration, heterogeneous distribution of ferrite particles, or limitations of the measurement conditions. Therefore, the EDX results provide partial elemental evidence supporting the composite composition, while additional characterization is required to confirm the presence of Ni and the formation of the intended ferrite phase.

3.4. N_2 physisorption (BET) analysis

N_2 physisorption at 77.35 K revealed marked differences among the samples (**Fig. 6, Table 1**). The cellulose-derived carbon (750 °C) was practically non-porous, with a BET surface area of 0.37 $m^2\ g^{-1}$, a total pore volume of 0.0117 $cm^3\ g^{-1}$, and a mean pore diameter of 127 nm. Its negative BET C constant (−13.9) indicates that the BET model is not strictly applicable at such a low surface area, and the values are therefore reported as indicative only. The pristine $NiCuFe_2O_4$ exhibited a type II/III isotherm with H3-type hysteresis,

typical of slit-shaped voids between aggregated spinel nanoparticles, and a low surface area of 7.088 $m^2 g^{-1}$, consistent with the magnetic dipole–dipole agglomeration of ferrites (Fig. 6a)

In contrast, the $NiCuFe_2O_4$/ACCell composite displayed a hybrid type I/IV isotherm: a steep uptake at $p/p_0 < 0.05$, indicating micropore filling, followed by a hysteresis loop (closest to H4) with an abrupt closure at $p/p_0 \approx 0.42–0.5$, characteristic of narrow slit-like mesopores (Fig. 6c). The BET surface area reached 72.32 $m^2 g^{-1}$ (Vm = 16.62 $cm^3 g^{-1}$), with a Langmuir area of 92.57 $m^2 g^{-1}$, a total pore volume of 0.0767 $cm^3 g^{-1}$, and a mean pore diameter of 4.24 nm. The high and positive C constant (487) reflects strong adsorbate–surface interaction associated with microporosity; consequently, the BET area is regarded as an apparent value.

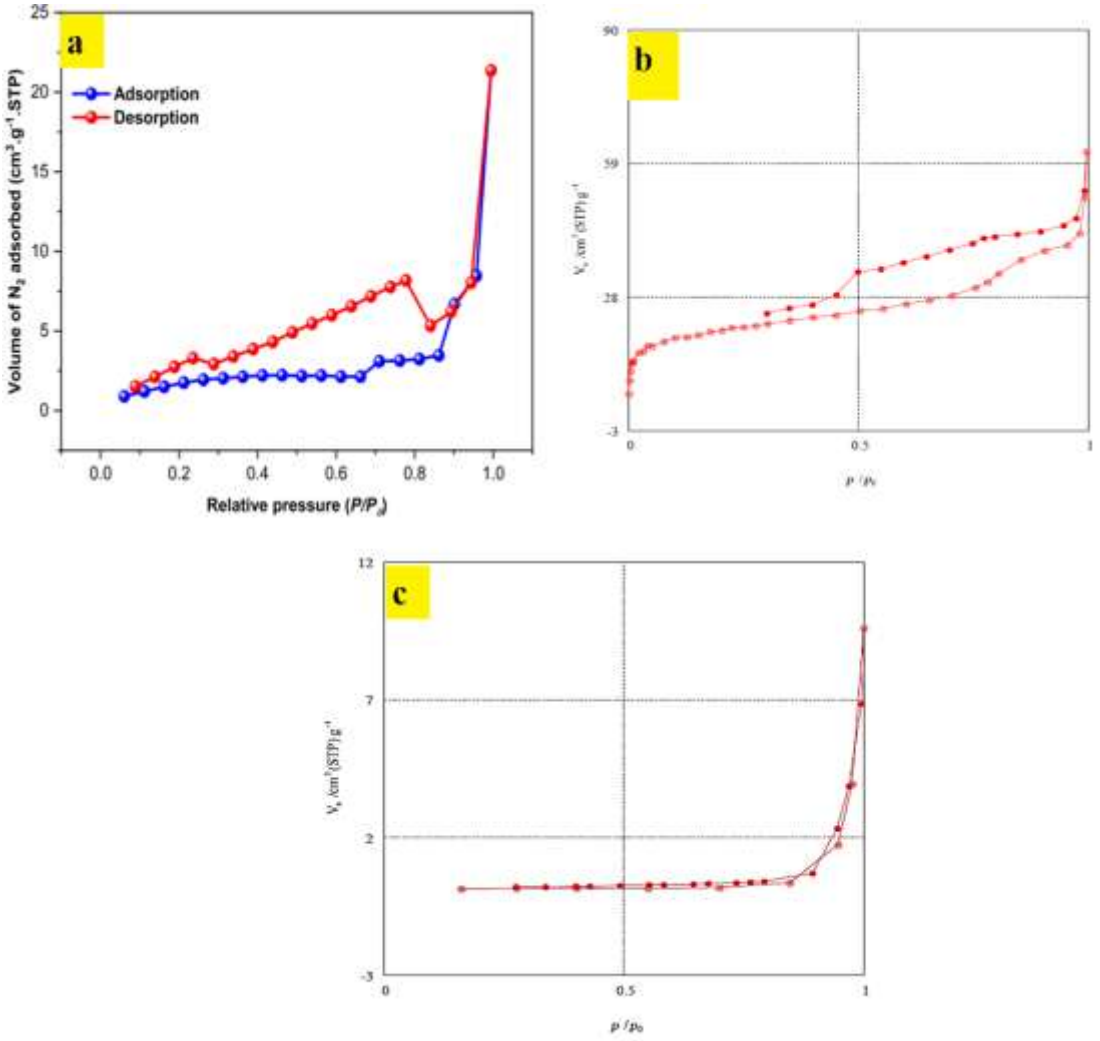


Figure 6. N_2 adsorption–desorption isotherm curves (a)NCF , (b) ACCell, and (c) NCF/ACCell nanocomposite, respectively.

The BJH mesopore area (31.5–39.0 $m^2 g^{-1}$; Vp ≈ 0.058–0.059 $cm^3 g^{-1}$) was considerably smaller than the BET area, indicating that a substantial part of the surface is contributed by micropores. The BJH adsorption branch showed a broad mesopore band centered at a pore radius of about 5 nm (diameter ≈ 10 nm), whereas the sharp desorption maximum at 1.85 nm is attributed to forced pore closure (tensile-strength effect) rather than to a real pore population.

The roughly 200-fold increase in surface area relative to the carbon support cannot be explained by simple additivity of the components. It is attributed to the dispersion of ferrite nanoparticles on the ACCell-derived matrix, which suppresses aggregation and generates interparticle micro- and mesovoids; a catalytic contribution of Ni, Cu, and Fe

during the thermal treatment may also play a role, which should be supported by the SEM and XRD results. This hierarchical micro/mesoporous texture provides more accessible active sites and shorter diffusion paths for pollutant molecules, which is expected to enhance dye adsorption and photocatalytic efficiency, in addition to the electronic and optical effects discussed in the preceding sections.

Table 1. Textural parameters of the investigated samples derived from N_2 adsorption–desorption at 77.35 K.

Parameter	**Cellulose-derived carbon (750 °C)**	**$NiCuFe_2O_4$**	**$NiCuFe_2O_4$/** ACCell
Isotherm / hysteresis	II/III, negligible	II/III, H3	I/IV, H4
S_{BET} ($m^2\ g^{-1}$)	0.37	7.088	72.32
C_{BET}	−13.9 (invalid)	-	486.99
$S_{Langmuir}$ ($m^2\ g^{-1}$)	0.69	-	92.57
V_t at $p/p_0 = 0.990$ ($cm^3\ g^{-1}$)	0.0117	-	0.0767
Mean pore diameter, 4V/A (nm)	127.0	1.752	4.24

3.5. Photocatalytic degradation of methylene blue

The efficiency of photodegradation of methylene blue (MB) via the photocatalysis method in an aqueous environment using direct exposure was evaluated based on its interaction with the NCF/ACCell binary photocatalyst. Based on the absorbance results, it can be seen that the strength of the main peak of MB (λmax = 664 nm) decreases with time when exposed to the binary NCF/ACCell. The NCF/ACCell photocatalyst achieved a degradation efficiency of 91% after 44 min at pH = 7 and an MB concentration of 15 mg L^{-1}, which increased to 97% under alkaline conditions (pH 10). Numerous factors contribute to the enhancement of the photocatalytic efficacy of the NCF/ACCell photocatalyst, including a substantial surface area characterized by a mesoporous architecture and the presence of oxygen-containing functional groups that may reduce agglomeration and offer additional active sites for optimal photon absorption.

The rate of MB dye photodegradation was determined from the plot of ln(Ci/Ct) vs. irradiation time and was linear, giving an R^2 value of 0.984. As shown in Figure 7, the reactions follow pseudofirst order kinetics, as expressed below [28, 29]:

$$ln(C_i/C_t) = kt \quad \ldots \quad (2)$$

In which Ci stands for the initial concentration of MB dye, Ct stands for the concentration of MB at different time intervals, k is the rate constant of the photodegradation reaction in min^{-1}, and t is the time of irradiation in minutes. NCF/ACCell nanocomposite has a rate constant of 0.0428 min^{-1}. The increased rate constant in case of the binary NCF/ACCell nanocomposite may be due to the formation of reactive species like hydroxyl free radicals (•OH) and superoxide anions (O_2•$^-$), which cause the degradation of MB pollution and also high efficiency of electron-hole separation in case of NCF/ACCell catalyst.

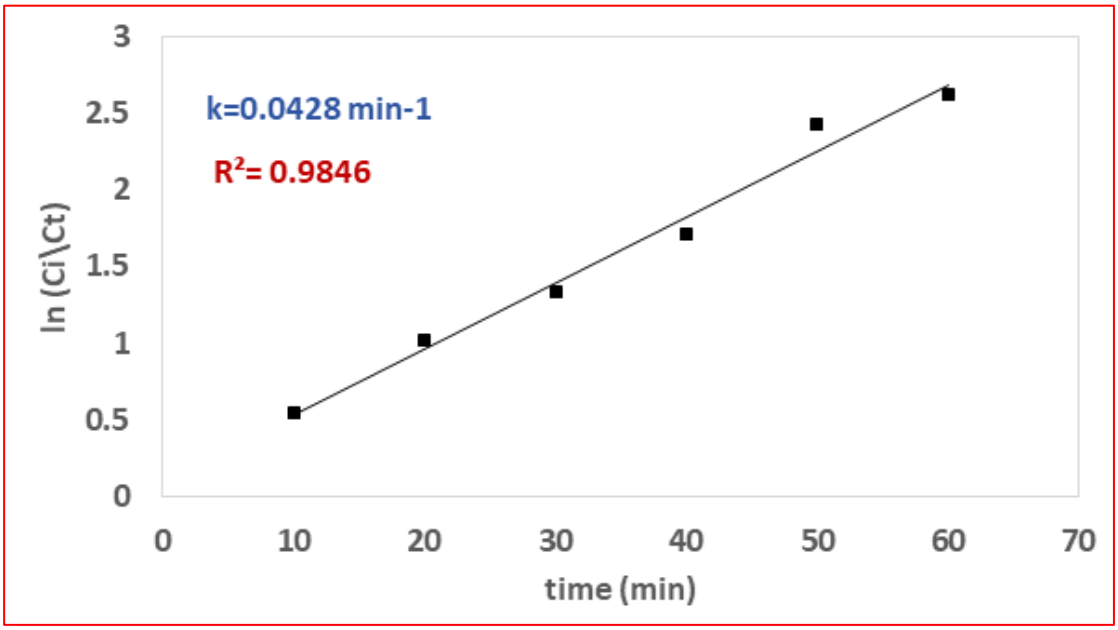


Figure 7. kinetic plots of MB dye degradation

The impact of different dosages of the photocatalyst, reaction solution pH, and MB concentration was investigated for the achievement of the most effective photodegradation of the MB pollutant by the newly designed NCF/ACCell photocatalyst. Figure 8a presents the effect of reaction solution pH on the degradation efficiency of the MB pollutant by the catalyst within the pH range of 2-10 using dilution of HCl and NaOH solutions under similar conditions as mentioned above. As can be seen from the obtained graph, the catalyst has poor photocatalytic efficiency at acidic pH (pH = 2, 48%). On the other hand, the photocatalytic efficiency is greatly enhanced at alkaline pH (pH = 6, 91% and pH = 10, 97%).

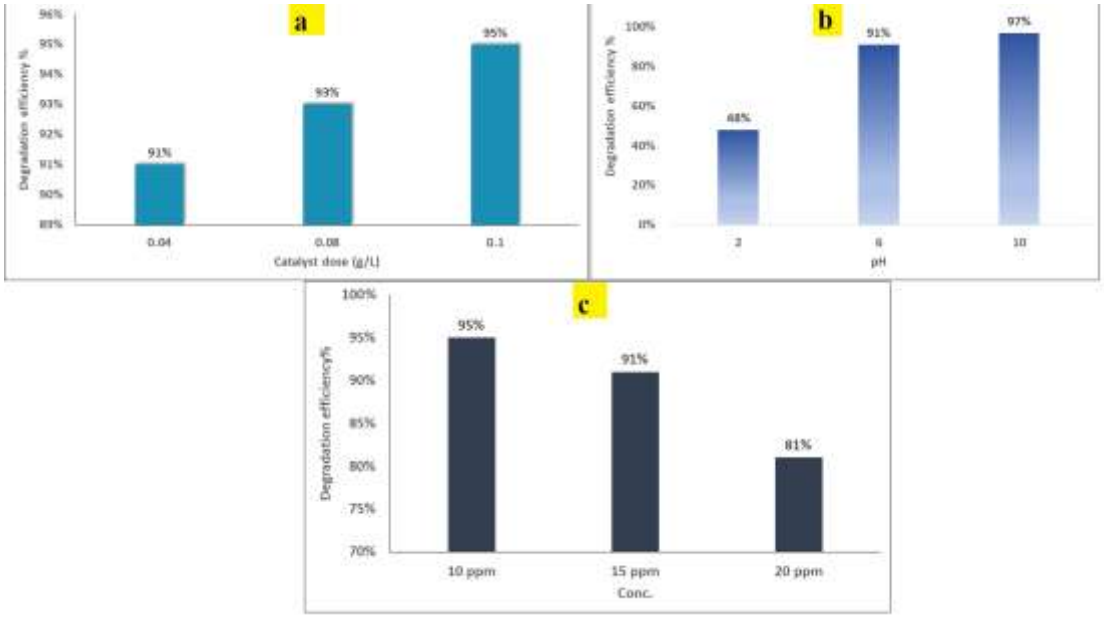


Figure 8. (a) Dose of the Catalyst (g) (pH = 7, and dye concentration = 15 mg/L) (b) Graphs depicting MB dye degradation efficiency at 1 h due to (a) pH (dye concentration = 15 mg/L, and catalyst dose = 0.04 g) (, and (c) Concentration of MB dye (mg/L) (Catalyst dose = 0.04 g, and pH = 7).

The reduced photodegradation in the case of reduced pH values is explained due to the distribution of positive charges on the surface of the catalyst that causes an excess of

H^+ ions; therefore, there is an electrostatic hindrance for the adsorption of cationic MB dye. On the other hand, at alkaline pH values, the highest adsorption takes place between the cationic MB dye and the photocatalyst. This can be explained due to the presence of a negative charge on the surface of the catalyst as a result of OH^- ions, causing electrostatic attraction of cationic MB dye to the surface of the catalyst [19]. Fig. 8b illustrates the varying effects of catalyst dosage on the photodegradation efficacy of MB dye; the results indicate that the degradation efficiency increased from 91% at 0.04 g/L to 93% at 0.08 g/L and 95% at 0.1 g/L. Although the highest efficiency was observed at 0.1 g/L, the dosage of 0.04 g/L was selected as optimal for subsequent experiments owing to the marginal improvement at higher doses, which does not justify the additional material consumption. The dye concentration in the wastewater has significant effects on the photocatalysis efficiency. For this reason, the following three dye concentrations were chosen and illuminated using visible light irradiation for 50 minutes each with a catalyst concentration of 0.04 g/L and pH of 7, as shown in Figure 8(c). The degradation efficiency was 95% at 10 mg/L, 91% at 15 mg/L, and 81% at 20 mg/L. The decrease at higher concentrations is attributed to the limited number of active sites and the screening effect of the dye molecules, which reduces the number of photons reaching the catalyst surface and consequently the formation of e^-/h^+ pairs.

4. Conclusions

Cellulose-derived activated carbon, $NiCuFe_2O_4$, and the $NiCuFe_2O_4$/ACCell nanocomposite was successfully synthesized via the sol-gel auto-combustion technique. The incorporation of cellulose-derived activated carbon dramatically narrowed the band gap of $NiCuFe_2O_4$ from 2.896 eV to 1.566 eV, thereby extending light absorption into the visible region. The nanocomposite exhibited a hierarchical micro/mesoporous texture with a BET surface area of 72.32 $m^2\ g^{-1}$, providing abundant active sites and short diffusion paths for pollutant molecules. The NCF/ACCell photocatalyst achieved a degradation efficiency of 97% for methylene blue within 50 min under alkaline conditions (pH 10), following pseudo-first-order kinetics with a rate constant of 0.0428 min^{-1}. The enhanced photocatalytic performance is attributed to the synergistic effects of band-gap narrowing, improved surface area, and efficient electron–hole separation. These findings confirm that the $NiCuFe_2O_4$/ACCell nanocomposite is a highly promising, economical, and sustainable photocatalyst for the remediation of organic dye contaminants in wastewater. Further studies are recommended to evaluate its reusability and performance under real wastewater conditions.

REFERENCES

[1] A. Negash, S. Mohammed, H. D. Weldekirstos, A. D. Ambaye, and M. Gashu, "Enhanced photocatalytic degradation of methylene blue dye using eco-friendly synthesized rGO@ZnO nanocomposites," *Scientific Reports*, vol. 13, Art. no. 22234, 2023.

[2] J. Liu, D. Zhang, X. Pu, D. Dong, P. Cai, and H. J. Seo, "Combustion synthesis and photocatalytic properties of magnetically separable Zn1−xCdxS/γ-Fe2O3 composites," *Materials Letters*, vol. 130, pp. 94–96, 2014.

[3] V. Vaiano, O. Sacco, D. Sannino, and P. Ciambelli, "Process intensification in the removal of organic pollutants from wastewater using innovative photocatalysts obtained coupling zinc sulfide based phosphors with nitrogen doped semiconductors," *Journal of Cleaner Production*, vol. 100, pp. 208–211, 2015.

[4] J. Liang, Y. Wei, J. Zhang, Y. Yao, G. He, B. Tang, and H. Chen, "Scalable green method to fabricate magnetically separable NiFe2O4-reduced graphene oxide nanocomposites with enhanced photocatalytic performance driven by visible light," *Industrial & Engineering Chemistry Research*, vol. 57, no. 12, pp. 4311–4319, 2018.

[5] K. Tikoo, "Enhanced catalytic activity of composites of NiFe2O4 and nano cellulose derived from waste biomass for the mitigation of organic pollutants," *Arabian Journal of Chemistry*, 2017.

[6] T. A. Khan, A. S. Saud, S. S. Jamari, M. H. Ab Rahim, J. W. Park, and H. J. Kim, "Hydrothermal carbonization of lignocellulosic biomass for carbon rich material preparation: A review," *Biomass and Bioenergy*, vol. 130, Art. no. 105384, 2019.

[7] A. I. Osman, A. Abdelkader, C. Farrell, D. Rooney, and K. Morgan, "Reusing, recycling and up-cycling of biomass: A review of practical and kinetic modelling approaches," *Fuel Processing Technology*, vol. 192, pp. 179–202, 2019.

[8] S. Phromphithak, T. Onsree, and N. Tippayawong, "Machine learning prediction of cellulose-rich materials from biomass pretreatment with ionic liquid solvents," *Bioresource Technology*, vol. 323, Art. no. 124642, 2021.

[9] Y. D. Chai, Y. L. Pang, S. Lim, W. C. Chong, C. W. Lai, and A. Z. Abdullah, "Recent progress on tailoring the biomass-derived cellulose hybrid composite photocatalysts," *Polymers*, vol. 14, no. 23, Art. no. 5244, 2022.

[10] H. Wang et al., "Semiconductor heterojunction photocatalysts: Design, construction, and photocatalytic performances," *Chemical Society Reviews*, vol. 43, no. 15, pp. 5234–5244, 2014.

[11] C. Cao, L. Xiao, C. Chen, and Q. Cao, "Synthesis of novel Cu2O/BiOCl heterojunction nanocomposites and their enhanced photocatalytic activity under visible light," *Applied Surface Science*, vol. 357, pp. 1171–1179, 2015.

[12] M. A. Mohamed et al., "An overview on cellulose-based material in tailoring bio-hybrid nanostructured photocatalysts for water treatment and renewable energy applications," *International Journal of Biological Macromolecules*, vol. 103, pp. 1232–1256, 2017.

[13] M. Du, Y. Du, Y. Feng, Z. Li, J. Wang, N. Jiang, and Y. Liu, "Advanced photocatalytic performance of novel BiOBr/BiOI/cellulose composites for the removal of organic pollutant," *Cellulose*, vol. 26, no. 9, pp. 5543–5557, 2019.

[14] Y. Ren, Q. Dong, J. Feng, J. Ma, Q. Wen, and M. Zhang, "Magnetic porous ferrospinel NiFe2O4: A novel ozonation catalyst with strong catalytic property for degradation of di-n-butyl phthalate and convenient separation from water," *Journal of Colloid and Interface Science*, vol. 382, no. 1, pp. 90–96, 2012.

[15] L. Sun, R. Shao, L. Tang, and Z. Chen, "Synthesis of ZnFe2O4/ZnO nanocomposites immobilized on graphene with enhanced photocatalytic activity under solar light irradiation," *Journal of Alloys and Compounds*, vol. 564, pp. 55–62, 2013.

[16] H. Y. Zhu, R. Jiang, S. H. Huang, J. Yao, F. Q. Fu, and J. B. Li, "Novel magnetic NiFe2O4/multi-walled carbon nanotubes hybrids: Facile synthesis, characterization, and application to the treatment of dyeing wastewater," *Ceramics International*, vol. 41, no. 9, pp. 11625–11631, 2015.

[17] T. J. Al-Musawi, P. Rajiv, N. Mengelizadeh, F. S. Arghavan, and D. Balarak, "Photocatalytic efficiency of CuNiFe2O4 nanoparticles loaded on multi-walled carbon nanotubes as a novel photocatalyst for ampicillin degradation," *Journal of Molecular Liquids*, vol. 337, Art. no. 116470, 2021.

[18] G. Sharma, V. K. Gupta, S. Agarwal, S. Bhogal, M. Naushad, A. Kumar, and F. J. Stadler, "Fabrication and characterization of trimetallic nano-photocatalyst for remediation of ampicillin antibiotic," *Journal of Molecular Liquids*, vol. 260, pp. 342–350, 2018.

[19] I. F. Waheed, M. M. Awsaj, O. S. Dahham, M. Q. Jabbar, F. M. Al-Abady, and M. A. F. Al-Samarrai, "Synthesis of CoMnFe2O4 hollow microstructure decorated GO for photocatalytic degradation of organic dyes," *Arabian Journal of Chemistry*, vol. 17, no. 9, Art. no. 105934, 2024.

[20] M. Rahimi, M. Hashemi, and A. Nasiri, "ZnCoFe2O4@MC/WO3 anchored on multi-walled carbon nanotubes (MWCNT) as a cutting-edge heterogeneous nanocatalyst for cefixime degradation in wastewater: Synthesis, characterization, antibacterial activity and mechanism study," *Journal of Environmental Chemical Engineering*, vol. 13, no. 5, Art. no. 117424, 2025.

[21] R. Khalifeh, M. Rajabzadeh, and A. Ebadi, "Triple-shell hollow CuNiFe2O4 spheres as heterogeneous catalyst for selective oxidation of alcohols," *ChemistrySelect*, vol. 4, no. 45, pp. 13089–13093, 2019.

[22] H. Ji et al., "Magnetic g-C3N4/NiFe2O4 hybrids with enhanced photocatalytic activity," *RSC Advances*, vol. 5, no. 71, pp. 57960–57967, 2015.

[23] H. Ahamad, N. Meshram, S. Bankar, S. Dhoble, and K. Rewatkar, "Structural properties of CuxNi1−xFe2O4 nano ferrites prepared by urea-gel microwave auto combustion method," *Ferroelectrics*, vol. 516, pp. 67–73, 2017.

[24] L. Gan et al., "The fabrication of bio-renewable and recyclable cellulose based carbon microspheres incorporated by CoFe2O4 and the photocatalytic properties," *Journal of Cleaner Production*, vol. 196, pp. 594–603, 2018.

[25] I. F. Waheed, M. A. Hamad, K. A. Jasim, and A. J. Gesquiere, "Degradation of methylene blue using a novel magnetic CuNiFe2O4/g-C3N4 nanocomposite as heterojunction photocatalyst," *Diamond and Related Materials*, vol. 133, Art. no. 109716, 2023.

[26] H. Helmiyati, N. Fitriana, M. L. Chaerani, and F. W. Dini, "Green hybrid photocatalyst containing cellulose and γ-Fe2O3-ZrO2 heterojunction for improved visible-light driven degradation of Congo red," *Optical Materials*, vol. 124, Art. no. 111982, 2022.

[27] H. Hamad, E. Bailón-García, S. Morales-Torres, F. Carrasco-Marín, A. F. Pérez-Cadenas, and F. J. Maldonado-Hódar, "Functionalized cellulose for the controlled synthesis of novel carbon-Ti nanocomposites: Physicochemical and photocatalytic properties," *Nanomaterials*, vol. 10, no. 4, Art. no. 729, 2020.

[28] M. S. Athar, M. Danish, and M. Muneer, "Fabrication of visible light-responsive dual Z-Scheme (α-Fe2O3/CdS/g-C3N4) ternary nanocomposites for enhanced photocatalytic performance and adsorption study in aqueous suspension," *Journal of Environmental Chemical Engineering*, vol. 9, no. 4, Art. no. 105754, 2021.

[29] S. Qi, D. Wang, Y. Zhao, and H. Xu, "Core-shell g-C3N4@Zn0.5Cd0.5S heterojunction photocatalysts with high photocatalytic activity for the degradation of organic dyes," *Journal of Materials Science: Materials in Electronics*, vol. 30, no. 5, pp. 5284–5296, 2019.

[30] M. S. Anwar et al., "Electronic properties of composite iron (II, III) oxide (Fe3O4) carbonaceous absorber materials by electron spectroscopy," *Journal of Electron Spectroscopy and Related Phenomena*, vol. 229, pp. 47–51, 2018.

[31] Q. Wang, H. Yue, T. Du, W. Zhang, Y. Qiao, H. Dong, Y. Yin, and S. Yang, "A particle-carbon matrix architecture for long-term cycle stability of ZnFe2O4 anode," *RSC Advances*, vol. 6, no. 41, pp. 35110–35117, 2016.

[32] D. Varghese, M. Joe Raja Ruban, P. Joselene Suzan Jennifer, D. AnnieCanisius, S. Chakko, S. Muthupandi, J. Madhavan, and M. Victor Antony Raj, "Comprehensive analysis of NiFe2O4/MWCNTs nanocomposite to degrade a healthcare waste-tetracycline," *RSC Advances*, vol. 13, pp. 28339–28361, 2023.

[33] L. T. T. Nguyen, A. T. T. Duong, N. D. Bui, V. T. M. Ngo, H. Q. Nguyen, H. T. T. Nguyen, G. T. Tran, and T. V. Tran, "Synthesis of magnetic NiFe2O4/g-C3N4 heterojunction photocatalysts for boosting dye degradation performance under visible-light irradiation," *Nanoscale Advances*, vol. 7, pp. 536–548, 2025.